The effect of oxygen fugacity on the rheological evolution of crystallizing basaltic melts

S. Kolzenburg [a,c,*], D. Di Genova [b], D. Giordano [c], K.U. Hess [a], D.B. Dingwell [a]

[a] *Department für Geo- und Umweltwissenschaften, Ludwig-Maximilians-Universität, 80333 München, Germany*
[b] *School of Earth Sciences, University of Bristol, BS8 1RJ Bristol, United Kingdom*
[c] *Dipartimento di Scienze della Terra, Università degli Studi di Torino, 10125 Torino, Italy*

A B S T R A C T

Storage and transport of silicate melts in the Earth's crust and their emplacement on the planet's surface occur almost exclusively at sub-liquidus temperatures. At these conditions, the melts undergo crystallization under a wide range of cooling-rates, deformation-rates, and oxygen fugacities (fO_2). Oxygen fugacity is known to influence the thermodynamics and kinetics of crystallization in magmas and lavas. Yet, its influence on sub-liquidus rheology remains largely uncharted.

We present the first rheological characterization of crystallizing lavas along natural cooling paths and deformation-rates and at varying fO_2. Specifically, we report on apparent viscosity measurements for two crystallizing magmatic suspensions 1) at log fO_2 of -9.15 (quartz–fayalite–magnetite buffer, QFM, -2.1) and 2) in air. These fugacities span a range of reduced to oxidized conditions pertinent to magma migration and lava emplacement. We find that: 1) crystallization at constant cooling-rates results in a quasi-exponential increase in the apparent viscosity of the magmatic suspensions until they achieve their rheological cut off temperature (T_{cutoff}), where the melt effectively solidifies 2) the rheological departure and T_{cutoff} increase with increasing fO_2 and 3) increasing fO_2 results in decreased crystallization-rates. Based on the experimental results and by comparison with previous rheological isothermal studies we propose a generalisation of the effect of fO_2 on the dynamic rheological evolution of natural magmatic and volcanic suspensions. We further discuss the implications for magmatic transport in plumbing and storage systems (e.g. conduits, dikes and magma chambers) and during lava flow emplacement.

© 2018 The Authors. Published by Elsevier B.V. This is an open access article under the CC BY-NC-ND license (http://creativecommons.org/licenses/by-nc-nd/4.0/).

1. Introduction

1.1. Motivation and scope of this study

Basaltic compositions represent the most abundant volcanism on Earth and other terrestrial bodies such as the Moon and Mars (Chevrel et al., 2013a; Sigurdsson et al., 2015). Their eruptions can drastically alter global climate and lead to regional disruption of agriculture and aviation (Sigurdsson et al., 2015). Understanding their flow behaviour and emplacement mechanisms informs the prediction of volcanic hazards and risks. It also informs the deduction of lava compositions and associated environmental parameters of planetary volcanism.

Magma is forced towards the surface by buoyancy forces resulting from the density contrast with the host rock (Sigurdsson et al., 2015). Its migration in the crust and emplacement on the surface are governed by its effective viscosity (Chevrel et al., 2015; Kolzenburg et al., 2017; La Spina et al., 2016; Nicolas and Ildefonse, 1996; Pinkerton and Sparks, 1978; Sato, 2005; Vona and Romano, 2013), the flow/effusion-rate (Harris and Rowland, 2009; Nicolas and Ildefonse, 1996), the plumbing system geometry (La Spina et al., 2015) and the underlying topography (Cashman et al., 2013; Kolzenburg et al., 2016a). Forecasting the flow behaviour of magmas and lavas, to date, is hindered most severely by an incomplete understanding of how lava-rheology evolves during emplacement and when flow ceases (Chevrel et al., 2013b; Giordano et al., 2007; Kolzenburg et al., 2017).

Predicting the flow dynamics of magmas and lavas relies thus on a detailed understanding of their rheology, which evolves during migration, eruption and emplacement. This evolution in rheology is caused by changes in phase state, melt composition, texture and temperature of the magma resulting from gas loss, cooling and crystallization. This creates strongly heterogeneous flow conditions, textures and morphologies (Arzilli and Carroll, 2013; La Spina et al., 2016; Nicolas and Ildefonse, 1996; Shaw et al., 1968; Sigurdsson et al., 2015; Vetere et al., 2017) that evolve in space

and time. Understanding the rheological evolution of crystallizing magmas/lavas requires direct measurement of the flow properties at emplacement conditions. Few direct measurements of lava rheology under natural conditions are reported (Pinkerton and Sparks, 1978; Shaw et al., 1968). These measurements are crucial for benchmarking of experimental data, but insufficient to develop a systematic understanding of the evolution of lava-flow properties in response to varying external and internal parameters (composition, cooling- and shear-rate, oxygen fugacity etc.), as they represent snapshots of the system at one specific condition.

Magmas are generated in the Earth's interior at low oxygen fugacities (fO_2) and then transported to and erupted on the Earth's surface where they encounter increasingly oxidizing conditions. The effect of oxygen fugacity on the transport properties of natural silicate melts at super-liquidus temperatures has been investigated for a range of compositions (Chevrel et al., 2013a; Dingwell, 1989; Dingwell and Virgo, 1987; Mysen et al., 1984; Sato, 2005).

However, migration and transport of magma generally occurs in settings where the melts crystallize. Oxygen fugacity affects the stability of Fe-bearing phases, the crystallization- and degassing-onset, -path and -kinetics and the glass transition (Tg) of magmas under both static (i.e. constant T and P) and dynamic (decreasing P and T) conditions (Arzilli and Carroll, 2013; Bouhifd et al., 2004; Hamilton et al., 1964; La Spina et al., 2016; Markl et al., 2010; Sato, 1978; Toplis and Carroll, 1995).

Crystallization, in turn, increases the effective magma viscosity and therewith influences its migration and the eruptive style of volcanoes. This sparked a series of sub-liquidus rheology experiments on a variety of compositions, dominantly basaltic and andesitic. This is because they provide favourable crystallization kinetics, resulting in a manageable time frame of experimentation (Bouhifd et al., 2004; Chevrel et al., 2015; Sato, 2005; Vetere et al., 2017; Vona and Romano, 2013; Vona et al., 2011; Wilke, 2005). Most existing rheological data stem from measurements at constant temperature and atmospheric conditions (i.e. equilibrated in air) that may not necessarily be representative of the dynamic emplacement situations in nature. Evaluating the influence of the evolving flow properties of lavas on their emplacement dynamics requires characterization of the rheological properties of lavas at non-isothermal and non-equilibrium conditions. In such conditions, the lava undergoes transient increases in viscosity, reaching increasing degrees of undercooling until a "rheological cut off temperature" (T_{cutoff}) (Giordano et al., 2007; Kolzenburg et al., 2016b, 2017) is reached, where the effective viscosity rises steeply, terminating its capacity to flow. This transient rheological gradient governs the lavas' emplacement. Studies on the effect of oxygen fugacity on the sub-liquidus rheological evolution of magmas/lavas are scarce (Bouhifd et al., 2004; Sato, 2005) and few measurements of the cooling-rate dependent, disequilibrium rheology of natural melts exist to date (Giordano et al., 2007; Kolzenburg et al., 2016b, 2017). In fact, to our knowledge no study on the effect of oxygen fugacity on the disequilibrium rheology of natural melts under either static or dynamic thermal conditions has been presented.

We present the first dataset on the sub-liquidus rheological evolution of Etna and Holuhraun melts during crystallization at reduced conditions and in air. Reduced experiments are performed at low $\log fO_2$ with respect to magmatic conditions to assess the maximum possible effect that changes in fO_2 may have on the systems' crystallization dynamics and rheological evolution.

1.2. The role of iron in melt-structure and eruptive dynamics

The role of iron in silicate melt structure and viscosity has been extensively investigated via experiments (Di Genova et al., 2017b; Dingwell and Virgo, 1987; Giordano et al., 2015; Mysen et al., 1984; Poe et al., 2012; Toplis and Carroll, 1995). Viscosity models, such as (Giordano et al., 2008b; Russell et al., 2003), however, generally do not include this effect. This is largely because most studies do not report iron speciation for the investigated melts and the understanding of the structural role of iron in melts, especially during migration and eruption remains incomplete (Cicconi et al., 2015; Giordano et al., 2015; Poe et al., 2012; Wilke, 2005). Based on literature results, it is generally accepted that the iron coexists in both reduced (FeO) and oxidized (Fe_2O_3) states with coordination environments ranging from tetrahedral to pentahedral and octahedral depending on the melt composition, temperature and oxygen fugacity (Mysen et al., 1984; Wilke, 2005). Because of this unique behaviour, several studies show that increasing Fe_2O_3 content, during magma ascent and oxidation, results in increasing melt viscosity (Bouhifd et al., 2004; Di Genova et al., 2017b). However, the structural role (i.e. network former vs network modifier) of iron is still highly debated (Alderman et al., 2017; Poe et al., 2012) and *in-situ* studies such as Cicconi et al. (2015) are required to better constrain the iron environment in melts, especially in dynamic temperature and fO_2 conditions.

Iron oxidation state also shifts phase equilibria (Hamilton et al., 1964; Markl et al., 2010), influencing the magmas' crystallization path (Toplis and Carroll, 1995) and rheological evolution (Bouhifd et al., 2004; Sato, 2005). Moreover, it has been demonstrated that changing the dissolved iron content in melts is responsible for iron nanolite formation which, in turn, affects the viscosity and may facilitate the exsolution of volatiles (Di Genova et al., 2017a).

2. Physical constraints on the ascent and emplacement conditions of basaltic magma

Common oxygen fugacities for basaltic lava flows and shallow magmatic systems at eruptive temperatures lie in the range of $\log fO_2 = -8$ to -11 (nickel–nickel oxide buffer (NNO) to QFM -1) (Hamilton et al., 1964; Markl et al., 2010; Mollo et al., 2015; Sato, 1978).

Once flowing towards the surface, lavas are exposed to increasingly oxidizing conditions and fO_2 starts to equilibrate towards atmospheric values. Redox equilibration of silicate melts in experiments occurs on the timescale of hours to days (Dingwell and Virgo, 1987; Mysen et al., 1985). In most lavas, especially ones that crystallize rapidly, redox equilibrium with the atmosphere is unlikely to be achieved. Experiments performed under equilibrated atmospheric conditions, therefore, represent an end-member case at the most oxidized conditions to be expected in nature.

Coherent basaltic (low viscosity) magmas rising in a conduit or in narrow and shallow dikes commonly undergo cooling-rates from few degrees per hour to $\sim 10\,^{\circ}C\,min^{-1}$ (Giordano et al., 2007; La Spina et al., 2015, 2016), due to thermal exchange with the conduit wall and gas expansion and escape. These cooling-rates represent steady flow conditions after an initial rapid chilling event of the first batch of magma of up to $50\,^{\circ}C\,min^{-1}$ (Giordano et al., 2007). However, in extreme events, such as basaltic plinian eruptions (Schauroth et al., 2016), high flux-rates may result in heating of the conduit walls. The data presented here are, therefore only to be applied to emplacement conditions where the thermal history can be constrained. Cooling-rates of basalts, measured in active lava channels range from 0.01 to $15\,^{\circ}C\,min^{-1}$, where high cooling-rates represent the exterior and lower values the insulated interior of the lava (Cashman et al., 2013; Kolzenburg et al., 2017; Witter and Harris, 2007).

Shear-rates during viscous transport in dike, conduit, or storage systems range from $\sim 70\,s^{-1}$ in plinian eruptions (Papale, 1999) to as low as $10^{-9}\,s^{-1}$ in convecting magma chambers (Nicolas and Ildefonse, 1996). Effusion-rates for basaltic eruptions

range between 10–1000 $m^3 s^{-1}$ e.g. (Harris and Rowland, 2009). For common lava flow geometries (heights between 2 and 10 m; widths between 200–1000 m) this translates to shear-rates between ~0.001–2.5 s^{-1}. Shear-rates reconstructed for the eruption at Holuhraun lie in an intermediate field of 0.05 s^{-1} for the widest and 0.26 s^{-1} for the most narrow flow sections (Kolzenburg et al., 2017). Shear-rates for eruptions at Etna are expected to be higher than for Holuhraun due to the steeper topographic relief.

The cooling- and shear-rates applied here are chosen to span the widest range of what is experimentally accessible using this setup (cooling-rates of 0.5–3 °C min^{-1}; initial shear-rates of 2.12 s^{-1} and 0.77 s^{-1} for the Etna and Holuhraun melts, respectively; see section 3.4, Dingwell and Virgo (1987) and Kolzenburg et al. (2017) for details). This represents the rapid to intermediate cooling-rates present in the conduits (La Spina et al., 2015, 2016), the interior of high aspect ratio (i.e. sheet-like) lava flows and the lava carapace (Kolzenburg et al., 2017; Witter and Harris, 2007), and the conditions of migrating magmas at shallow depths (La Spina et al., 2015). We chose two end-member fO_2 states (equilibrated at atmospheric conditions and log $fO_2 = -9.15$, (i.e. NNO+0.4) to simulate the oxidized and reduced conditions encountered by lavas during emplacement.

We acknowledge that the range of cooling- and shear-rates in nature, for instance during lava flow emplacement (Witter and Harris, 2007), span a wider range than what is possible to reproduce in the laboratory and that changes in both may further influence the investigated process.

3. Sample preparation and experimental method

3.1. Sample selection and geological relevance

Two melt compositions are chosen for this study: 1) a primitive basalt from the 2014–2015 eruption at Holuhraun, representing rift-zone volcanism and 2) a more evolved trachybasalt, sampled from the summit lava-flows of the November 2013 eruption of Etna, representing subduction zone volcanism. The results presented here are, therefore, useful for the interpretation of a large variety of magmatic and volcanic processes in a range of tectonic settings.

3.2. Sample preparation and compositional analysis

Rock samples are crushed and powdered using a jaw crusher and carbide ring-mill. The powders are then melted in large (100 ml), thin-walled, Pt crucibles in a Nabertherm® MOSi$_2$ box furnace at 1350 °C in batches of ~10 g, added to the crucible every 5 min. This avoids overflow of the melt due to foaming. Rock powders vesiculate during synthesis and produce a bubbly melt that loses its vesicles after ~20 min at 1350 °C. Vesiculation is likely due to a combination of the expansion of gas trapped in pores between sintering/agglutinating particles, the presence of moisture in the rock powder, the exsolution of dissolved volatiles from the partially glassy rock and the liberation of oxygen bubbles as the melt undergoes a change in redox state (Dingwell and Virgo, 1987; Sato, 1978). Once filled, the crucible is left in the furnace for about an hour to allow degassing. The total melting time is on the order of 3–5 h. Large volumes of melt were prepared in Fe saturated crucibles so that Fe-loss is negligible. Diffusive loss of volatile elements negligible due to 1) low melting temperatures 2) short melting timescales and 3) the small surface to volume ratio, where the loss of volatile elements is compensated by the large sample volume. The samples are quenched to glasses by pouring them onto a steel plate. The glasses are crushed and re-melted into Pt$_{80}$Rh$_{20}$ cylindrical crucibles of 51 mm height and 26.6 mm diameter for viscometry.
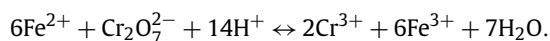
Table 1
Composition of both samples in this study as wt% oxides measured after the experiments; normalized to 100% (EPMA totals are reported below; analytical precision is better than 2.5%).

Oxide	Holuhraun	Etna
SiO$_2$	49.74	48.01
TiO$_2$	1.81	1.90
Al$_2$O$_3$	13.75	17.20
FeO	12.01	10.94
MnO	0.23	0.07
MgO	6.97	4.99
CaO	12.43	10.58
Na$_2$O	2.70	3.58
K$_2$O	0.21	2.11
P$_2$O$_5$	0.16	0.62
Fe^{2+}/FeO$_{tot}$@1320 °C CO/CO$_2$ = 40/60	0.75	0.63
Fe^{2+}/FeO$_{tot}$@1320 °C in Air	0.56	0.39
Analytical total	99.80	97.25

The composition of the glasses is measured with a Cameca SX100 electron probe micro-analyser (EPMA). Analyses are carried out at 15 kV acceleration voltage and, to minimise the alkali loss, a defocused beam (10-µm) and 5 nA beam current is used. Calibration standards are wollastonite (Ca, Si), periclase (Mg), hematite (Fe), corundum (Al), natural orthoclase (K), and albite (Na). The precision is better than 2.5% for all analysed elements. The homogeneity of the glasses is verified by performing around 15 analyses per sample. The compositions of both glasses are reported in Table 1.

3.3. Iron redox titration

Iron redox state measurements are performed on dip quench samples using potassium dichromate titration. The sample material is digested in concentrated sulfuric (H$_2$SO$_4$) and hydrofluoric (HF) acids. The method was calibrated against iron(II) ethyldiammoniumsulfate and the amount of Fe^{2+} is determined via the following redox reaction:

$$6Fe^{2+} + Cr_2O_7^{2-} + 14H^+ \leftrightarrow 2Cr^{3+} + 6Fe^{3+} + 7H_2O.$$

These data are used in combination with the EPMA analyses to calculate the Fe^{2+}/FeO$_{tot}$ ratio for each glass. The analytical results are reported in Table 1.

3.4. Concentric cylinder viscometry experiments

Concentric cylinder viscometry represents a widely-applied technique for measuring the viscosity of silicate melts at superliquidus temperatures (Chevrel et al., 2013a, 2015; Dingwell, 1989; Dingwell and Virgo, 1987; Giordano et al., 2007, 2008a; Kolzenburg et al., 2016b, 2017; Sato, 2005; Vetere et al., 2017; Vona and Romano, 2013; Vona et al., 2011). The samples are stirred at ambient pressure and a constant temperature of 1359 °C (equivalent to a furnace set point of 1375 °C; see Kolzenburg et al. (2016b) for calibration procedure) for several hours to ensure chemical and thermal homogeneity, which is confirmed by constant torque and temperature readings. The furnace temperature is then decreased in steps of 25 °C and held until a steady temperature and torque reading is achieved (typically ~45 min). These data are used to recover the samples' super-liquidus viscosity at atmospheric conditions.

For constant cooling-rate experiments, each cooling-rate is calibrated separately because the measurement systems' thermal inertia creates unique thermal conditions (initial thermal lag and thermal offset between sample and furnace temperature during cooling). Details on the experimental procedure for constant-cooling

experiments, device calibration and the limitations of this method are presented in section 5.4 of this contribution, and Kolzenburg et al. (2016b, 2017). The precision of these viscosity measurements is ±3% (Dingwell and Virgo, 1987, 2016b). Detailed descriptions of the gas mixing furnace and its use in viscometry experiments can be found in Dingwell and Virgo (1987) and Chevrel et al. (2013a).

The same samples used to measure liquid viscosity at isothermal conditions are also used for dynamic cooling sub-liquidus experiments. Measurements are performed by imposing constant cooling-rates of 0.5, 1, and 3 °C min^{-1} and a mean initial shear-rates of 0.77 and 2.12 s^{-1} for the Holuhraun and Etna melts, respectively. The difference in initial shear-rate is a result of using different spindle geometries for each melt, an experimental necessity arising from the different absolute viscosities of the two samples. It also reflects the natural emplacement situation, where lava flows on Etna are emplaced at higher shear-rates due to the steeper emplacement surface. Measurements on the Holuhraun melt are performed using a large bob spindle with 14.3 mm diameter and 33.9 mm height, whereas measurements on the Etna melt are performed using a small bob spindle with 3.2 mm diameter and 42 mm height. Both spindles have 45° conical tips to reduce edge effects (Dingwell and Virgo, 1987). During the cooling experiments the measured torque constantly increases as a function of the increasing apparent viscosity of the suspension. The Brookfield DV-III+ viscometer head used in these experiments has a maximum torque capacity of 0.7187 mNm and the shear-rate is automatically halved every time this limit is reached.

After each experiment, and before running the next one, the sample is re-heated to 1320 °C for a minimum of 2–7 h. The samples are homogenized by stirring at the initial shear-rate (0.77 and 2.12 s^{-1} for Holuhraun and Etna, respectively) in order to ensure melting of the crystalline phases formed during previous experimentation. The homogenization time is set to be longer than the duration of previous experiment to ensure redox re-equilibration. Crystallization experiments last between 0.5 and 6.5 h (during which the melt is at lower temperatures, i.e. higher viscosities and slower redox equilibration) and we therefore assume that the melt's redox state re-equilibrated to the initial, pre-experimental state within the re-equilibration time. This assumption is supported by the observation that torque values measured after re-homogenization between and after all experimental runs stabilize with a reproducibility of ~1.5% of the measured value.

After performing all crystallization experiments in air, the samples are heated to 1320 °C and the melt is reduced by flowing a CO/CO$_2$ mixture through the alumina muffle tube at a ratio of 40/60. The total gas flow-rate is set to 100 ml min^{-1} using Tylan electronic mass flow controllers to ensure that no atmospheric oxygen can influence the fugacity conditions dictated by the CO/CO$_2$ reaction balance. Mysen et al. (1984) report complete redox equilibration in droplet-sized samples of iron rich silicate melts to occur within less than 30 min, whereas Dingwell and Virgo (1987) report that for sample of the same volume as used in this study, complete redox equilibration may take up to 24 h for samples with slightly higher iron contents than the ones used here. Chevrel et al. (2013a) measured iron-rich basaltic analogues for Martian melts and report equilibration after 24 h.

The samples are stirred at a shear-rate of 0.77 and 2.12 s^{-1} for the Holuhraun and Etna melts, respectively for a minimum of 36 h to ensure complete redox equilibration. Equilibrium is confirmed by a constant torque reading for over 5 h. Dip quench samples of each melt are taken after redox equilibration to determine the Fe^{2+}/Fe$_{tot.}$ ratio; see Table 1. The liquid viscosity measurement is performed as described above for atmospheric conditions. The sample used for all the constant cooling-rate experiments is re-melted and quenched to a glass after the end of the last cycle.

3.5. Suspension vs. liquid viscosity and the effect of changing melt composition during crystallization

The viscosity of magmas/lavas is highly temperature dependent and increases by several orders of magnitude with decreasing temperature. This is a result of the combined effects of the temperature dependent viscosity of the silicate melt and the effect of increasing solid fraction in the suspension during crystallization.

Isolating the effect of crystal growth on the apparent viscosity of the magmatic suspension requires a model of the theoretical temperature–viscosity relationship of the pure melt. To do so, a Vogel Fulcher Tammann (VFT)-model is fit to the pure liquid high and low T viscosity measurements. The data of the crystallization experiments is normalized to this model using the following equation:

$$\eta_r = \frac{\eta_s}{\eta_l} \tag{1}$$

where η_r, η_s and η_l are the relative viscosity, the viscosity of the suspension (i.e. liquid plus crystals) and the liquid viscosity, respectively. Direct ties between relative viscosity data and crystal content in this type of experiment are hindered by the fast nucleation and growth kinetics that change with decreasing temperature. The imposed cooling-rates push the melt to continuously higher degrees of undercooling until wholesale matrix crystallization occurs at T_{cutoff}. This is discussed in more detail in section 5.4.2.

Liquid models (Giordano et al., 2008a; Russell et al., 2003) are created via interpolation of super liquidus viscosity measurements with either low temperature measurements, e.g. via micro–penetration viscometry (e.g. Giordano et al., 2008b and references therein) or estimation of the melt viscosity by application of a shift factor to differential thermal analysis data (Giordano et al., 2008a) using a Vogel–Fulcher–Tammann (VFT) equation. Here we measure the glass transition temperature (T_g) of samples quenched at varying oxidation states using a Netzsch Pegasus 404 differential scanning calorimeter (DSC). The samples are first annealed via heating and cooling at a constant-rate of 10 °C min^{-1} to cancel the thermal history of the sample acquired during quenching. Glass transition measurements are then performed at a heating-rate of 10 °C min^{-1} in an Ar-atmosphere. We correlate onset ($T_{g_{onset}}$) and peak ($T_{g_{peak}}$) from these measurements to the melts viscosity following the method of Giordano et al. (2008a). These data, together with the high temperature viscosity measurements and VFT-model parameters are presented in the results section. The VFT fit parameters obtained from fitting the viscosity measurements are well within the range expected for basaltic compositions (Giordano et al., 2008b; Russell et al., 2003).

Crystallization induces changes in the residual melt composition by removing certain components from the melt to form crystals. This effect is largest once the melt and crystals are in thermodynamic equilibrium at atmospheric fO_2 conditions, since they favour crystallization (Gualda and Ghiorso, 2015; Markl et al., 2010; Mysen et al., 1985; Toplis and Carroll, 1995). This state is, however, never reached during constant cooling experiments because they are continuously driven to higher undercooling. Any effect of changing melt composition in these experiments is, therefore, smaller than it would be at equilibrium conditions. In order to assess the maximum effect of changing interstitial melt composition on the measured data we model the equilibrium melt composition at the lowest experimental temperatures (1044 °C for Holuhraun and 984 °C for Etna) using MELTS software (Gualda and Ghiorso, 2015) and calculate its viscosity at the experimental temperature using Giordano et al. (2008b). We do so because 1) it allows assessing the maximum possible effect (i.e. at equilibrium
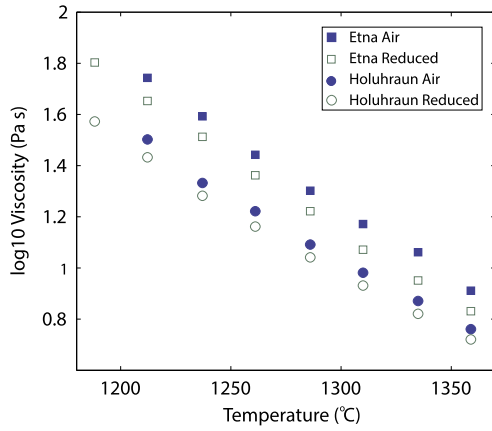
Fig. 1. Liquid viscosity data. Viscosity measurements, of the super-liquidus viscosity of the Holuhraun (circles) and Etna (squares) melts at reduced conditions (open) and in air (filled). Melt viscosity is lower for the reduced melts, this effect is larger for the Etna than the Holuhraun melt.

Fig. 2. Evolution of apparent viscosity of the crystalizing melts. Summary of the measured apparent viscosities from dynamic crystallization experiments of the (A) Holuhraun and (B) Etna melts at varying cooling-rates and oxygen fugacities including the VFT-model fitted to the liquid viscosity data of Table 2. Note that all samples follow the VFT model up until the point where the presence of crystals becomes significant enough to influence the flow behaviour of the sample.

conditions) and 2) direct sampling and measurement of the interstitial melt composition is not possible with sufficient accuracy in these type experiments; see section 5.4.2 for details.

The viscosities of the original- and the equilibrium fractionated melt compositions at 60 vol. % crystallinity and QFM-2 vary within less than 0.6 and 0.14 log units for the Etna and Holuhraun melts, respectively. We can, therefore, exclude drastic effects of changing melt composition on the rheological measurements and attribute changes in relative viscosity over the experimental temperature interval to crystallization (i.e. the increasing solid fraction in the suspension).

4. Results

4.1. Liquid viscosity

The results of the liquid viscosity measurements and low temperature model estimates for both melts are summarized in Table 2 together with the VFT model parameters. High Temperature viscosity measurements are plotted in Fig. 1. Increasing $f O_2$ (i.e. oxidation) increases the super-liquidus viscosity of both melts. This increase is between 0.08–0.11 log units for the Etna melt and between 0.04 and 0.07 log units for the Holuhraun melt. This viscosity increase is tied to the polymerisation of the melt, as network modifying, five- and/or six fold coordinated Fe^{2+}; is oxidised to tetrahedral Fe^{3+} shown in Table 1.

No constant torque reading is achieved for temperatures below 1188 °C at reduced conditions and 1212 °C in air for both melts, suggesting slow crystallization of the sample. This is supported by the observation that when revisiting higher temperatures, reproducible, steady measurements can be achieved. Since data from unsteady torque measurements are no longer a measure of pure melt viscosity but a melt–crystal suspension, data below these temperatures are discarded.

4.2. Dynamic crystallization experiments

The experimental data for both magmatic suspensions, at varying cooling-rates, are plotted in Fig. 2. Initially, they follow the trend of the pure liquid data (and extrapolated VFT fit for the supercooled liquid), resulting in a zero (0) $\log \eta_r$ (Fig. 3). Once the crystallinity becomes sufficiently high to measurably influence the melt-viscosity, the apparent viscosity of the suspension increases with respect to the theoretical liquid (i.e. η_r increases). This deviation from the pure liquid model occurs at different degrees of undercooling (i.e. below the liquidus temperature) depending
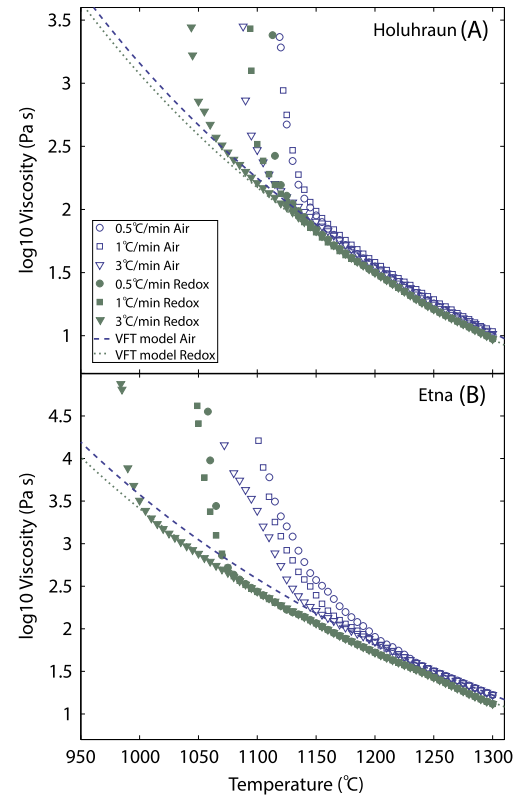
on the applied cooling-rate. It is at the lowest temperature for the fastest cooling-rate and increases with decreasing cooling-rate. These changes in relative viscosity (η_r) are directly linked to the rate of crystallisation, since increases in relative viscosity result from a larger fraction of crystals, impeding flow.

The following sections detail the respective changes for both investigated melts and their dependence on oxygen fugacity. For comparative analysis the rheological departure is defined as the point at which the relative viscosity exceeds all potential influences of noise in the data ($\eta_r > 0.25$). The experimental T_{cutoff} is defined as the temperature at which the measurements approach the torque limit of the respective measuring geometry ($\log \eta_s > 3.5$ for the large bob geometry – Holuhraun melt; $\log \eta_s > 4.5$ for the small bob geometry – Etna melt).

4.2.1. Holuhraun

Figs. 2A and 3A show the measured apparent viscosity and the calculated relative viscosity for the Holuhraun melt as a function of temperature, respectively. The experimental data are reported both as log absolute and log relative viscosity in Tables 3 and 4, respectively. At reduced conditions, the departure from the pure liquid model ($\log \eta_r > 0.25$) occurs at 1066, 1119 and 1127 °C for cooling-rates of 3, 1 and 0.5 °C min^{-1}, respectively. The relative viscosity then increases quasi exponentially until they reach their respective experimental T_{cutoff} ($\log \eta_s > 3.5$) at 1044, 1094 and 1113 °C for cooling-rates of 3, 1 and 0.5 °C min^{-1}, respectively.

At oxidising conditions, in air, both the departure and the final T_{cutoff} values are shifted to higher temperatures. The departure from the pure liquid model ($\log \eta_r > 0.25$) is shifted by 17, 30 and 44 °C and occurs at 1110, 1149 and 1144 °C for cooling-rates of 3, 1 and 0.5 °C min^{-1}, respectively. The experimental T_{cutoff}

Table 2
Summary of liquid viscosity measurements (high temperatures) and model estimates of the low temperature viscosity of the melt and VFT-fit parameters.

Temperature		Holuhraun		Etna	
(K)	(C)	Air	Reduced	Air	Reduced
			log 10 Viscosity (Pa s)		
1632	1359	0.76	0.72	0.91	0.82
1608	1335	0.87	0.82	1.06	0.95
1583	1310	0.98	0.93	1.17	1.07
1559	1286	1.09	1.04	1.30	1.22
1534	1261	1.22	1.16	1.44	1.36
1510	1237	1.33	1.28	1.59	1.51
1485	1212	1.50	1.43	1.74	1.65
1461	1188		1.57		1.80
917	644	11.98[a]			
951	678	10.56[a]			
914	641		11.98[a]		
954	681		10.56[a]		
922	649			11.98[a]	
959	686			10.56[a]	
920	647				11.98[a]
963	690				10.56[a]
VFT-model parameters	A	−3.34	−3.28	−3.98	−3.71
	B	3985	3852	5006	4541
	C	660	666	610	635

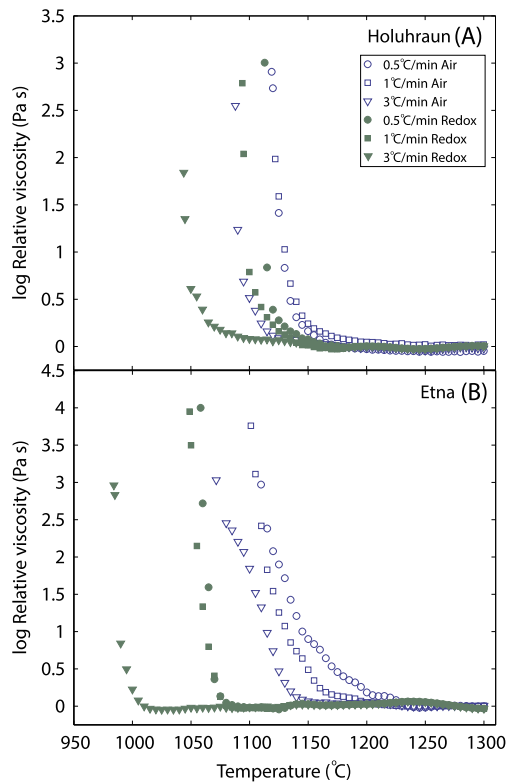[a] Calculated after Giordano et al. (2008a).

Fig. 3. Evolution of relative viscosity of the crystalizing melt. Summary of the calculated relative viscosities from dynamic crystallization experiments of the (A) Holuhraun and (B) Etna melts at varying cooling-rates and oxygen fugacities.

($\log \eta_s > 3.5$) are shifted by 5, 19 and 44 °C to 1088, 1113 and 1118 °C for cooling-rates of 3, 1 and 0.5 °C min^{-1}, respectively.

4.2.2. Etna

Figs. 2B and 3B show the measured absolute apparent viscosity and the calculated relative viscosity for the Etna melt as a function of temperature, respectively. The experimental data are reported in Tables 3 and 4, respectively. At reduced conditions the departure

from the pure liquid model ($\log \eta_r > 0.25$) is quasi exponential and occurs at 999, 1073 and 1072 °C for cooling-rates of 3, 1 and 0.5 °C min^{-1}, respectively. The experimental T_{cutoff} ($\log \eta_s > 4.5$) are reached at 984, 1050 and 1058 °C for cooling-rates of 3, 1 and 0.5 °C min^{-1}, respectively.

In air both the departure and the final T_{cutoff} values are shifted to higher temperatures. The departure from the pure liquid model ($\log \eta_r > 0.25$) is shifted by between 86 and 135 °C and occurs at 1134, 1159 and 1196 °C for cooling-rates of 3, 1 and 0.5 °C min^{-1}, respectively. The relative viscosity then assumes a quasi linear increase until they reach their respective experimental T_{cutoff} ($\log \eta_s > 4.5$) occur at 1064, 1097 and 1180 °C for cooling-rates of 3, 1 and 0.5 °C min^{-1}, respectively, corresponding to a shift of 22 to 74 °C.

5. Discussion

5.1. The effect of fO_2 on the disequilibrium rheology of basaltic melts

Under both reduced and oxidized conditions, faster cooling-rates drive the onset of crystallization to lower temperatures and the crystallization-rate (i.e. the steepness of the rheological departure) increases with increasing undercooling for both melts. Under reduced conditions, this departure occurs at lower temperatures than under oxidizing conditions for both melts.

However, although the difference in Fe-content between these two melts is small (∼1%; Table 1), increasing oxygen fugacity affects the two melts differently. For the Holuhraun melt, the shift in rheological departure and the experimental T_{cutoff} is less pronounced (max. 44 degrees at a cooling-rate of 3 °C min^{-1}) than for the Etna melt (135 and 74 degrees on onset and T_{cutoff}, respectively at a cooling-rate of 3 °C min^{-1}); see Figs. 2 and 3. These shifts become less intense with decreasing cooling-rate. The larger effect of changing fO_2 on the Etna melt suggests that its structure is more dependent on the Fe^{3+}/Fe$_{\text{tot}}$ ratio than that of the Holuhraun melt, where a decrease in iron in its network modifying state (Fe^{2+}) results in smaller variations in T_{cutoff} (Figs. 2 and 3).

Further, increasing fO_2 affects the crystallization-rate of the two melts differently. While crystallization results in very similar rheological solidification patterns at reduced and oxidized conditions for the Holuhraun melt (see similar shapes in the relative

Table 3
Summary of apparent viscosity measurements all experiments. For simplicity, interpolated values of the experimental data at equal temperature steps are reported with exception of the final datapoint for each experiment; highlighted in grey. Temperatures related to those points are reported in the last two rows in Kelvin and Celsius, respectively.

Sample		Etna						Holuhraun					
Shear rate		2.12 s^{-1}						0.77 s^{-1}					
Cooling rate		0.5°C/min		1°C/min		3°C/min		0.5°C/min		1°C/min		3°C/min	
Atmosphere		Air	CO/CO$_2$	Air	CO/CO$_2$	Air	CO/CO$_2$	Air	CO/CO$_2$	Air	CO/CO$_2$	Air	CO/CO$_2$
Temperature		Absolute viscosity (log 10 Pa s)											
(K)	(C)												
1573	1300	1.22	1.12	1.23	1.12	1.22	1.12	1.00	0.97	1.03	0.98	1.02	0.97
1568	1295	1.25	1.15	1.25	1.15	1.25	1.15	1.02	1.00	1.06	1.00	1.04	1.00
1563	1290	1.28	1.18	1.28	1.18	1.28	1.18	1.05	1.02	1.08	1.02	1.07	1.02
1558	1285	1.31	1.21	1.31	1.21	1.31	1.21	1.08	1.05	1.10	1.05	1.09	1.05
1553	1280	1.33	1.24	1.33	1.24	1.33	1.24	1.10	1.07	1.13	1.07	1.12	1.07
1548	1275	1.36	1.27	1.36	1.27	1.36	1.27	1.13	1.09	1.15	1.09	1.14	1.09
1543	1270	1.39	1.30	1.39	1.30	1.39	1.30	1.15	1.11	1.18	1.11	1.16	1.11
1538	1265	1.42	1.33	1.42	1.33	1.42	1.33	1.17	1.14	1.21	1.14	1.19	1.14
1533	1260	1.45	1.37	1.45	1.37	1.45	1.37	1.20	1.16	1.23	1.16	1.21	1.16
1528	1255	1.47	1.40	1.48	1.40	1.48	1.40	1.23	1.19	1.25	1.19	1.23	1.19
1523	1250	1.50	1.43	1.51	1.43	1.51	1.43	1.26	1.21	1.29	1.21	1.26	1.21
1518	1245	1.53	1.46	1.54	1.46	1.54	1.46	1.28	1.24	1.31	1.24	1.29	1.24
1513	1240	1.56	1.49	1.57	1.49	1.57	1.49	1.31	1.26	1.34	1.26	1.32	1.26
1508	1235	1.60	1.52	1.60	1.52	1.60	1.52	1.34	1.29	1.37	1.29	1.35	1.29
1503	1230	1.65	1.55	1.63	1.55	1.63	1.55	1.37	1.32	1.40	1.32	1.38	1.32
1498	1225	1.70	1.58	1.66	1.58	1.67	1.58	1.39	1.35	1.43	1.35	1.41	1.35
1493	1220	1.74	1.60	1.70	1.60	1.71	1.60	1.42	1.38	1.46	1.38	1.44	1.38
1488	1215	1.79	1.63	1.73	1.63	1.74	1.63	1.46	1.41	1.49	1.41	1.46	1.41
1483	1210	1.82	1.66	1.77	1.66	1.78	1.66	1.49	1.44	1.52	1.44	1.50	1.44
1478	1205	1.86	1.69	1.81	1.69	1.82	1.69	1.52	1.47	1.55	1.47	1.53	1.47
1473	1200	1.91	1.72	1.85	1.72	1.85	1.72	1.55	1.50	1.58	1.50	1.55	1.50
1468	1195	1.97	1.75	1.89	1.75	1.88	1.75	1.58	1.53	1.61	1.53	1.59	1.53
1463	1190	2.03	1.79	1.94	1.79	1.91	1.79	1.61	1.56	1.65	1.56	1.62	1.56
1458	1185	2.08	1.82	1.98	1.82	1.94	1.82	1.65	1.59	1.68	1.58	1.65	1.59
1453	1180	2.14	1.85	2.02	1.85	1.98	1.85	1.68	1.62	1.72	1.61	1.69	1.62
1448	1175	2.20	1.88	2.06	1.88	2.01	1.89	1.72	1.65	1.76	1.64	1.72	1.65
1443	1170	2.27	1.92	2.10	1.92	2.05	1.92	1.76	1.69	1.80	1.67	1.76	1.68
1438	1165	2.35	1.95	2.15	1.95	2.09	1.95	1.80	1.72	1.84	1.71	1.79	1.72
1433	1160	2.44	1.99	2.21	1.99	2.13	1.99	1.85	1.76	1.88	1.74	1.83	1.75
1428	1155	2.51	2.03	2.29	2.03	2.17	2.03	1.90	1.80	1.93	1.78	1.87	1.79
1423	1150	2.57	2.07	2.39	2.06	2.21	2.06	1.95	1.85	1.99	1.82	1.90	1.83
1418	1145	2.65	2.11	2.50	2.10	2.26	2.10	2.02	1.89	2.06	1.86	1.94	1.87
1413	1140	2.78	2.14	2.58	2.14	2.31	2.14	2.09	1.94	2.16	1.90	1.98	1.90
1408	1135	2.92	2.17	2.67	2.17	2.38	2.17	2.20	1.99	2.28	1.96	2.02	1.94
1403	1130	3.08	2.19	2.80	2.20	2.47	2.21	2.38	2.05	2.47	2.01	2.06	1.98
1398	1125	3.20	2.22	2.92	2.23	2.58	2.24	2.67	2.11	2.75	2.06	2.10	2.02
1393	1120	3.32	2.27	3.09	2.27	2.74	2.28	3.28	2.19	2.94	2.13	2.15	2.05
1388	1115	3.49	2.31	3.25	2.31	2.89	2.32	3.37	2.42		2.20	2.20	2.09
1383	1110	3.79	2.36	3.55	2.35	3.08	2.36		3.38		2.28	2.28	2.13
1378	1105		2.40	3.90	2.39	3.20	2.40				2.38	2.37	2.17
1373	1100		2.44	4.21	2.43	3.39	2.44				2.52	2.47	2.21
1368	1095		2.48		2.47	3.53	2.48				3.10	2.59	2.25
1363	1090		2.53		2.52	3.63	2.52				3.43	2.86	2.30
1358	1085		2.58		2.57	3.74	2.56					3.45	2.35
1353	1080		2.64		2.62	3.83	2.61						2.39
1348	1075		2.72		2.72	4.16	2.66						2.45
1343	1070		2.86		2.88		2.70						2.51
1338	1065		3.44		3.10		2.74						2.57
1333	1060		3.98		3.38		2.79						2.67
1328	1055		4.55		3.78		2.83						2.78
1323	1050				4.41		2.88						2.86
1318	1045				4.62		2.93						3.22
1313	1040						2.97						3.44
1308	1035						3.02						
1303	1030						3.07						
1298	1025						3.12						
1293	1020						3.17						
1288	1015						3.23						
1283	1010						3.30						
1278	1005						3.39						
1273	1000						3.51						
1268	995						3.68						
1263	990						3.89						
1258	985						4.81						
							4.88						
T Final	°K	1331	1374	1322	1350	1257		1392	1386	1396	1368	1361	1317
	°C	1058	1101	1049	1077	984		1119	1113	1122	1094	1088	1044

Table 4

Summary of the calculated relative viscosities for all experiments. For simplicity, interpolated values of the experimental data at equal temperature steps are reported with exception of the final datapoint for each experiment; highlighted in grey. Temperatures related to those points are reported in the last two rows in Kelvin and Celsius, respectively.

Sample		Etna						Holuhraun					
Shear rate		2.12 s^{-1}						0.77 s^{-1}					
Cooling rate		0.5 °C/min		1 °C/min		3 °C/min		0.5 °C/min		1 °C/min		3 °C/min	
Atmosphere		Air	CO/CO_2	Air	CO/CO_2	Air	CO/CO_2	Air	CO/CO_2	Air	CO/CO_2	Air	CO/CO_2
Temperature (K)	(C)	Log (relative viscosity)											
1573	1300	0.00	−0.03	0.01	−0.03	0.01	−0.03	−0.05	0.00	0.02	0.01	−0.02	0.00
1568	1295	0.00	−0.03	0.00	−0.03	0.00	−0.03	−0.05	0.01	0.02	0.01	−0.02	0.01
1563	1290	0.00	−0.02	0.00	−0.02	0.00	−0.02	−0.05	0.01	0.00	0.01	−0.01	0.01
1558	1285	0.00	−0.02	0.00	−0.02	0.00	−0.02	−0.05	0.00	0.01	0.00	−0.01	0.00
1553	1280	0.01	−0.01	0.00	−0.01	0.00	−0.01	−0.06	0.00	0.02	0.00	−0.01	0.00
1548	1275	0.01	0.00	0.00	0.00	0.00	0.00	−0.05	0.00	0.01	0.00	−0.02	0.00
1543	1270	0.01	0.02	0.00	0.02	0.00	0.02	−0.06	−0.01	0.01	−0.01	−0.02	−0.01
1538	1265	0.01	0.03	0.00	0.03	0.00	0.03	−0.06	−0.01	0.02	−0.01	−0.03	−0.01
1533	1260	0.00	0.04	0.00	0.04	0.00	0.04	−0.05	−0.02	0.01	−0.02	−0.03	−0.02
1528	1255	−0.01	0.05	0.00	0.05	0.00	0.05	−0.06	−0.02	0.01	−0.02	−0.04	−0.02
1523	1250	−0.02	0.06	0.00	0.06	−0.01	0.06	−0.05	−0.02	0.02	−0.02	−0.04	−0.02
1518	1245	−0.02	0.06	0.00	0.06	−0.01	0.06	−0.06	−0.02	0.02	−0.02	−0.04	−0.02
1513	1240	−0.01	0.06	0.00	0.06	0.00	0.06	−0.05	−0.03	0.01	−0.02	−0.03	−0.03
1508	1235	0.01	0.06	0.00	0.06	0.00	0.06	−0.05	−0.02	0.02	−0.02	−0.03	−0.02
1503	1230	0.04	0.06	0.00	0.06	0.01	0.06	−0.05	−0.02	0.03	−0.02	−0.02	−0.02
1498	1225	0.08	0.05	0.01	0.05	0.02	0.05	−0.05	−0.01	0.03	−0.01	−0.02	−0.01
1493	1220	0.12	0.04	0.01	0.04	0.03	0.04	−0.04	−0.01	0.03	−0.01	−0.02	−0.01
1488	1215	0.14	0.04	0.02	0.04	0.04	0.04	−0.04	0.00	0.03	0.00	−0.02	0.00
1483	1210	0.13	0.03	0.02	0.03	0.05	0.03	−0.03	0.00	0.04	0.00	−0.02	0.00
1478	1205	0.15	0.03	0.03	0.03	0.05	0.03	−0.04	0.00	0.05	0.01	−0.01	0.00
1473	1200	0.18	0.03	0.05	0.03	0.05	0.03	−0.03	0.00	0.05	0.01	−0.01	0.00
1468	1195	0.26	0.02	0.07	0.02	0.05	0.02	−0.02	0.00	0.05	0.01	−0.01	0.00
1463	1190	0.32	0.02	0.10	0.02	0.04	0.02	−0.02	0.00	0.06	0.00	−0.01	0.00
1458	1185	0.35	0.02	0.11	0.02	0.03	0.02	−0.01	−0.01	0.07	−0.01	0.00	−0.01
1453	1180	0.40	0.02	0.13	0.02	0.03	0.02	0.00	−0.01	0.08	−0.02	0.01	−0.01
1448	1175	0.46	0.01	0.14	0.02	0.04	0.02	0.01	0.01	0.09	−0.03	0.01	0.00
1443	1170	0.53	0.01	0.16	0.02	0.04	0.02	0.02	0.01	0.11	−0.03	0.02	0.00
1438	1165	0.64	0.01	0.19	0.01	0.05	0.02	0.04	0.00	0.14	−0.02	0.03	0.01
1433	1160	0.76	0.01	0.24	0.02	0.05	0.02	0.07	0.03	0.16	−0.02	0.03	0.02
1428	1155	0.83	0.02	0.34	0.02	0.05	0.02	0.12	0.05	0.19	0.00	0.04	0.02
1423	1150	0.90	0.03	0.49	0.02	0.07	0.02	0.16	0.08	0.24	0.01	0.05	0.04
1418	1145	1.00	0.03	0.64	0.02	0.09	0.02	0.23	0.09	0.33	0.02	0.06	0.04
1413	1140	1.21	0.03	0.74	0.02	0.12	0.02	0.31	0.13	0.47	0.04	0.07	0.04
1408	1135	1.43	0.01	0.85	0.01	0.20	0.02	0.48	0.16	0.67	0.09	0.08	0.05
1403	1130	1.72	−0.02	1.07	0.00	0.31	0.00	0.83	0.21	1.03	0.13	0.08	0.06
1398	1125	1.90	−0.04	1.26	−0.02	0.47	−0.01	1.41	0.28	1.59	0.16	0.09	0.07
1393	1120	2.08	−0.03	1.54	−0.03	0.74	−0.01	2.73	0.39	1.99	0.23	0.12	0.06
1388	1115	2.38	−0.02	1.83	−0.03	0.98	0.00	2.91	0.84		0.31	0.16	0.08
1383	1110	2.97	−0.01	2.42	−0.03	1.33	−0.01		3.00		0.42	0.24	0.07
1378	1105		−0.02	3.11	−0.03	1.52	−0.01				0.57	0.38	0.08
1373	1100		−0.02	3.76	−0.02	1.84	−0.01				0.79	0.51	0.08
1368	1095		−0.01		−0.03	2.07	−0.02				2.04	0.69	0.09
1363	1090		0.00		−0.03	2.21	−0.02				2.79	1.24	0.11
1358	1085		0.02		−0.02	2.36	−0.02					2.55	0.14
1353	1080		0.05		0.00	2.46	−0.02						0.14
1348	1075		0.13		0.13	3.03	−0.01						0.18
1343	1070		0.36		0.41		−0.02						0.21
1338	1065		1.59		0.80		−0.02						0.26
1333	1060		2.72		1.34		−0.02						0.39
1328	1055		4.00		2.15		−0.03						0.53
1323	1050				3.50		−0.02						0.61
1318	1045				3.95		−0.03						1.35
1313	1040						−0.04						1.84
1308	1035						−0.05						
1303	1030						−0.04						
1298	1025						−0.05						
1293	1020						−0.04						
1288	1015						−0.03						
1283	1010						0.00						
1278	1005						0.08						
1273	1000						0.22						
1268	995						0.50						
1263	990						0.84						
1258	985						2.83						
							2.96						
Datapoint	°K		1331	1374	1322	1345	1257	1392	1386	1396	1368	1361	1317
	°C		1058	1101	1049	1072	984	1119	1113	1122	1094	1088	1044

viscosity curves; Fig. 3), it drastically changes the rheological solidification pattern of the Etna melt. Crystallization of the Etna melt under reduced conditions occurs sudden and produces an extremely rapid increase in relative viscosity. Under oxidized conditions, however, crystallization is sluggish and produces slow increases in relative viscosity (Fig. 3). The higher absolute temperatures of T_{cutoff} for the Etna melt at oxidized conditions suggest that the melt, although being more polymerized, is becoming less stable than at reduced conditions, where the crystallization effect remains low until it reaches a level of undercooling at which crystallization occurs at extremely high-rates.

5.2. Implications for magma migration and lava flow emplacement

Recent studies on the rheology of melts under disequilibrium conditions (Giordano et al., 2007; Kolzenburg et al., 2016b, 2017) show that rheological data from experiments at constant temperatures (Chevrel et al., 2015; Sato, 2005; Vetere et al., 2017; Vona and Romano, 2013; Vona et al., 2011), and the combination of petrologic model data with theoretical models of the effect of particles on the effective rheology of suspensions (Gualda and Ghiorso, 2015; Mader et al., 2013), are insufficient to capture the rheological evolution of natural silicate melts at dynamic thermal and shear-conditions pertinent to nature. This is because the combination of thermodynamic and suspension rheology models assumes that changes in a melt's rheological properties occur instantaneously with changes in temperature and, therewith, crystal content of the magma or lava. However, dynamic undercooling results in thermodynamic disequilibrium and incomplete crystallization of the lava. Therefore, the effective suspension viscosity for any given temperature is lower in disequilibrium than in equilibrium, which contributes to the underestimation of lava flow runout distances (Kolzenburg et al., 2017).

Recent studies have demonstrated that basalts undergo cooling rates of $\sim$0.5–5° min^{-1} during ascent (see e.g. La Spina et al., 2016; Giordano et al., 2007 and references therein). Moreover, disequilibrium crystallization can occur in the conduit affecting the rheology of the magma. Since the crystal and bubble contents of a magma dramatically affect its viscosity, disequilibrium rheology is expected to affect the eruptive style and the depth of magma fragmentation (La Spina et al., 2016). Based on our results, we found that, for example, at 1100 °C the anhydrous viscosity of the crystallizing Etna magma increases by $\sim$4 orders of magnitude during oxidation, because crystallization is suppressed at reduced conditions. This shift in crystallization behaviour and, therewith, the rheological departure is controlled by the increase of oxygen fugacity (Fig. 2B). Thus, our experimental dataset suggests that fO_2 must be considered when modelling explosive basaltic eruptions.

The range of cooling- and shear-rate and fugacity conditions investigated here range from heavily reduced conditions (log $fO_2 = -9.15$) of some magma chambers to the extremely oxidized conditions (air) of natural emplacement scenarios and span the thermal- and deformation-regime from magma migration at shallow depths to lava flows on the surface. The data show that oxidizing conditions cause an anticipation (i.e. shift to higher temperatures) of the rheological departure, the melts' T_{cutoff} and change the melts crystallization kinetics. Uncertainties in fO_2 may, therefore, contribute to discrepancy between modelled and observed lava flow runout distances.

In the light of the presented measurements, rheological data measured on crystalizing melts at oxidizing conditions in air (Giordano et al., 2007; Kolzenburg et al., 2016b, 2017) may serve to define the high temperature limit of the crystallization process, defining the upper limit for the respective lava's T_{cutoff}. The low temperature T_{cutoff} limit remains to be explored experimentally in
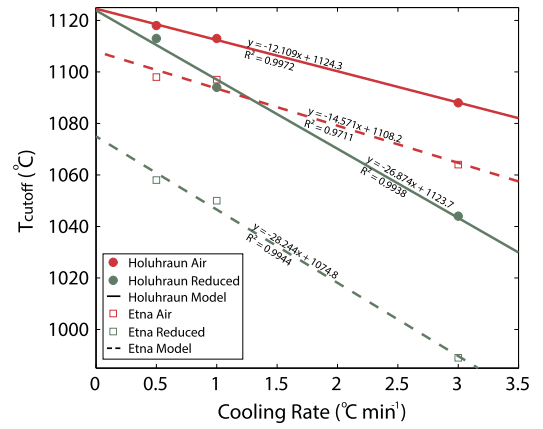

Fig. 4. T_{cutoff} as a function of cooling-rate for varying fO_2. T_{cutoff} for experiments on Holuhraun (circles) and Etna (squares) melts at log $fO_2 = -9.15$ (green, open) and in air (blue, filled). Linear fits to the data are presented as solid and dashed lines for the Holuhraun and Etna melts, respectively; green lines represent linear models of the experiments at log $fO_2 = -9.15$, blue lines to experiments in air. Note that with changing fO_2 both slope and absolute position of the models change with respect to the models of experiments at reduced conditions. However, the slope of both models are similar at similar fO_2 conditions. (For interpretation of the references to color in this figure legend, the reader is referred to the web version of this article.)

conjunction with measurements of oxygen fugacity of lava flows during emplacement.

5.3. Towards modeling the effect of oxygen fugacity on T_{cutoff}

Most natural lava emplacement process fall within the range of the experimental conditions presented here, including magmas erupted on Mars (Chevrel et al., 2015) and the presented results can inform on fugacity dependent changes.

To systematically describe the influence of fO_2 and cooling-rate on T_{cutoff} we plot the temperatures at which each experimental dataset passes a viscosity threshold beyond which the experiments reach the measurement limit of the device; i.e. the sample solidifies. This threshold is measurement geometry dependent and lies at log $\eta_s = 3.5$ Pa s for the setup used to measure the Holuhraun melt and log $\eta_s = 4.5$ Pa s for the setup used to measure Etna melt (Fig. 4).

We fit linear models to the data that describe T_{cutoff} as a function of cooling-rate with R-squared values of 0.971 to 0.997. The data show a steady decay of T_{cutoff} as a function of cooling-rate. This is due to the longer time spent at higher temperatures, allowing for crystal growth under near equilibrium conditions. However, both slope and temperature of T_{cutoff} change with fO_2. Besides increasing the absolute temperature of T_{cutoff}, increasing fO_2 serves to reduce the effect of cooling-rate. While the T_{cutoff} models have a steep slope of -26.9 and -28.2 for the Holuhraun and Etna melts at reduced conditions, respectively, they slope more gently at -12.1 to -14.6 for the Holuhraun and Etna melts, respectively, in air. This shows that cooling-rate has a more pronounced effect at reduced conditions (i.e. during magma rise and migration) than at oxidized conditions (i.e. during crust formation on lava flows).

To date, solidification thresholds used to determine whether a parcel in a flow model will behave solid (i.e. stop) or liquid (i.e. flow) are reported as 1) crystal volume fractions (Cashman et al., 1999; Costa et al., 2009; Harris and Rowland, 2001), 2) degree undercooling (Costa and Macedonio, 2005; Keszthelyi and Self, 1998) or 3) fixed temperatures (Costa and Macedonio, 2005; Del Negro et al., 2008; Spataro et al., 2010). Since cooling and changing fO_2 are inherent in nature, lava-flows will likely always have lower than equilibrium crystal contents.

No previous stopping criterion accounts for such cooling-rate and fO_2 dependent crystallization. This is likely the reason for the mismatches between predicted and observed lava flow runout distances because the temperature at which a given crystal volume fraction is present at disequilibrium is lower than modelled at equilibrium. The modelled runout distances, therefore, represent minimum values and actual distances are larger, highlighting the need for a composition-, oxygen fugacity- and cooling-rate dependent database to accurately model the flow properties of magmas and lavas under natural conditions. Incorporating such a database in magma migration and lava flow models would allow replacing the existing concepts of yield strength and other arbitrary or empirical stopping criteria with a melt specific parameter describing flow cessation as a function of composition and environmental parameters such as cooling-rate and fO_2. This would lead to a more realistic description of the magmas/lavas rheological evolution and therewith better ability to forecast their emplacement.

Models assessing ash dispersion and explosivity of basaltic magmas will also benefit from such data through the ability to generate more accurate source terms for the magmas evolving rheology during conduit transport and, therewith magma ascent-rates, see for example (La Spina et al., 2015, 2016). Here, the fO_2 and cooling-rate dependent viscosity evolution affects the modelled magma explosivity. This is because the documented changes in the effective magma viscosity (∼4 orders of magnitude during oxidation for the Etna melt) reduce the magmas ability to relax the imposed deformation-rates in a viscous manner.

However, since the presented T_{cutoff} models describe a crystallization induced rheological threshold, it is important to note that the model is only valid at sub-liquidus temperatures and non-equilibrium conditions.

5.4. Limitations of the data and method

5.4.1. Constraints on the applicability of the presented data

Both pressure and volatile content (H_2O and CO_2) may further affect the melts' crystallization-dynamics and rheological evolution. The experiments performed here are carried out on bubble-free melts at ambient pressures. This is important to consider when interpreting the data with respect to nature. They influence the effective viscosity of the magmatic suspension and its crystallization kinetics to varying degrees. With respect to the pure melt viscosity, the water content of the melt has the largest effect, where few weight percent water can decrease T_g of hundreds of degrees and viscosity by up to 6 orders of magnitude in rhyolites and 1.5 orders of magnitude for basalts (Di Genova et al., 2014; Giordano and Dingwell, 2003; Robert et al., 2008). Further, recent studies have shown that shear-rate may influence the crystallization kinetics of basaltic lavas at both isothermal (Vetere et al., 2017) and non-isothermal conditions (Kolzenburg et al., 2017) and more data are needed to constrain the magnitudes of this effect.

With respect to suspension rheology, increasing water content will push the onset of crystallization to lower temperatures, as shown in static crystallization experiments, e.g. (Arzilli and Carroll, 2013; Hamilton et al., 1964). Increasing pressure may change the crystallisation sequence e.g. (Arzilli and Carroll, 2013; Gualda and Ghiorso, 2015). However, to date, no experimental infrastructure exists to investigate these effects during rheological measurements. Gas exsolution and the production of vesicles can both increase and decrease the bulk viscosity of a suspension, depending on their capillary number (Llewellin and Manga, 2005; Mader et al., 2013).

5.4.2. Operational limitations of textural analyses

Contrary to previous rheological studies at constant temperatures, where sample textures evolve to an equilibrium that is quenched and analysed (Chevrel et al., 2013b, 2015; Sato, 2005; Vetere et al., 2017; Vona and Romano, 2013; Vona et al., 2011), our experiments are performed at constant cooling-rates. During constant cooling-rate experiments the degree of undercooling increases continuously and crystallization intensity increases throughout the experiment until the sample rheologically solidifies at T_{cutoff}. This serves to mimic natural conditions, where lavas, when erupted on the surface, constantly loose heat. The onset and evolution of the crystallization path, therefore, is not only dependent on the degree of undercooling and the melt's re-equilibration to this new temperature state but on the rate at which the undercooling is increased. At such dynamic conditions both, nucleation and growth kinetics are in competition with the changing temperature. Faster cooling-rates drive the melt to higher degrees of undercooling in shorter times than slow cooling-rates and crystal nucleation and growth struggle to keep up. This pushes the melt to continuously higher degrees of undercooling until wholesale matrix crystallization occurs at T_{cutoff}; see also Giordano et al. (2007), Kolzenburg et al. (2016b and 2017).

The nature of these experiments does not allow for sampling during experimentation, which would be necessary to correlate crystal volume fractions to the rheological data. Diffusion and crystal growth are very rapid in low viscosity melts and it is not possible to extract and quench the experimental charges fast enough to investigate their textures. Due to the high degree of undercooling the sample continues to crystalize at the extremely fast-rates as observed during the final phase of the experiment during extraction from the apparatus. Therefore, any correlation between the observed textures and the recorded data would be inaccurate. A decent quantification of textures during such rapidly evolving experiments would require high spatial and temporal resolution, in-situ tomographic data.

Albeit this type of experiment reduces the ability for detailed textural analyses, they have a significant advantage with respect to the study of the crystallization behaviour of the sample. Previous experiments at constant undercooling observed heterogeneous nucleation and growth of crystals preferentially at the crucible walls and the surface of the spindle; see for example (Chevrel et al., 2015; Sato, 2005; Vetere et al., 2017; Vona and Romano, 2013; Vona et al., 2011). This issue is most prominent at low degrees of undercooling because of the low degree of supersaturation (due to undercooling) of the respective phase. This results in low nucleation energy and preferential nucleation along material inhomogeneities such as the liquid solid interface at the crucible or spindle. In such a case, the effective spindle diameter increases (and effective crucible diameter decreases) and, therefore, the torque-viscosity calibration performed for a "naked" spindle and crucible geometry no longer holds. In the experiments performed here, however, crystallization occurs at significantly higher degrees of undercooling than in constant temperature experiments. This results in much higher nucleation and growth-rates than for "classic" experiments and rapid, quasi homogeneous, nucleation and rapid growth throughout the sample. This is supported by the rapid increase in apparent viscosity and shown previously via in-situ differential thermal analysis in Kolzenburg et al. (2016b). Therefore we deem any effect of heterogeneous nucleation and growth in these experiments negligible. They are therefore much less affected by changes in the experiment geometry.

6. Conclusions

Based on the data presented above and the accompanying analytical results we draw the following conclusions:

1. Changes in oxygen fugacity affect both the crystallization kinetics and T_{cutoff} of the lava, where more oxidizing conditions result in higher T_{cutoff} and lower crystallization intensity.
2. Even at similar total iron contents, the effect of increasing oxygen fugacity during ascent and eruption on the rheological solidification of lavas varies significantly with sample composition as a result of the changing melt structure.
3. The viscosity and, therewith, the explosive potential of basaltic melts at eruptive temperatures increases with increasing oxygen fugacity both through increases in the melt viscosity and promotion of dynamic crystallization.
4. The presented data are highlight the necessity of developing an empirical database of the temperature dependent viscosity of crystallizing silicate melts in dynamic temperature- and fO_2-space.
5. The presented data may be employed in physical property based models of magma ascent dynamic and lava flow emplacement to more accurately constrain their results.

Acknowledgements

References

Alderman, O., Wilding, M., Tamalonis, A., Sendelbach, S., Heald, S., Benmore, C., Johnson, C., Johnson, J., Hah, H.-Y., Weber, J., 2017. Iron K-edge X-ray absorption near-edge structure spectroscopy of aerodynamically levitated silicate melts and glasses. Chem. Geol. 453, 169–185.

Arzilli, F., Carroll, M.R., 2013. Crystallization kinetics of alkali feldspars in cooling and decompression-induced crystallization experiments in trachytic melt. Contrib. Mineral. Petrol. 166, 1011–1027.

Bouhifd, M.A., Richet, P., Besson, P., Roskosz, M., Ingrin, J., 2004. Redox state, microstructure and viscosity of a partially crystallized basalt melt. Earth Planet. Sci. Lett. 218, 31–44.

Cashman, K., Soule, S., Mackey, B., Deligne, N., Deardorff, N., Dietterich, H., 2013. How lava flows: new insights from applications of lidar technologies to lava flow studies. Geosphere 9, 1664–1680.

Cashman, K.V., Thornber, C., Kauahikaua, J.P., 1999. Cooling and crystallization of lava in open channels, and the transition of Pāhoehoe Lava to'A'ā. Bull. Volcanol. 61, 306–323.

Chevrel, M.O., Cimarelli, C., deBiasi, L., Hanson, J.B., Lavallée, Y., Arzilli, F., Dingwell, D.B., 2015. Viscosity measurements of crystallizing andesite from Tungurahua volcano (Ecuador). Geochem. Geophys. Geosyst. 16, 870–889. https://doi.org/10.1002/2014GC005661.

Chevrel, M.O., Giordano, D., Potuzak, M., Courtial, P., Dingwell, D.B., 2013a. Physical properties of $CaAl_2Si_2O_8$–$CaMgSi_2O_6$–FeO–Fe_2O_3 melts: analogues for extraterrestrial basalt. Chem. Geol. 346, 93–105. https://doi.org/10.1016/j.chemgeo.2012.09.004.

Chevrel, M.O., Platz, T., Hauber, E., Baratoux, D., Lavallée, Y., Dingwell, D.B., 2013b. Lava flow rheology: a comparison of morphological and petrological methods. Earth Planet. Sci. Lett. 384, 109–120.

Cicconi, M.R., Neuville, D.R., Tannou, I., Baudelet, F., Floury, P., Paris, E., Giuli, G., 2015. Competition between two redox states in silicate melts: an in-situ experiment at the Fe K-edge and Eu L3-edge. Am. Mineral. 100, 1013–1016.

Costa, A., Caricchi, L., Bagdassarov, N., 2009. A model for the rheology of particle-bearing suspensions and partially molten rocks. Geochem. Geophys. Geosyst. 10. https://doi.org/10.1029/2008GC002138.

Costa, A., Macedonio, G., 2005. Numerical simulation of lava flows based on depth-averaged equations. Geophys. Res. Lett. 32. https://doi.org/10.1029/2004GL021817.

Del Negro, C., Fortuna, L., Herault, A., Vicari, A., 2008. Simulations of the 2004 lava flow at Etna volcano using the magflow cellular automata model. Bull. Volcanol. 70, 805–812.

Di Genova, D., Kolzenburg, S., Wiesmaier, S., Dallanave, E., 2017a. A chemical tipping point governing mobilization and eruption style of rhyolitic magma. Nature. https://doi.org/10.1038/nature24488.

Di Genova, D., Romano, C., Alletti, M., Misiti, V., Scarlato, P., 2014. The effect of CO_2 and H_2O on Etna and Fondo Riccio (Phlegrean Fields) liquid viscosity, glass transition temperature and heat capacity. Chem. Geol. 377, 72–86.

Di Genova, D., Vasseur, J., Hess, K.-U., Neuville, D.R., Dingwell, D.B., 2017b. Effect of oxygen fugacity on the glass transition, viscosity and structure of silica- and iron-rich magmatic melts. J. Non-Cryst. Solids 470, 78–85.

Dingwell, D.B., 1989. Shear viscosities of ferrosilicate liquids. Am. Mineral., 1038–1044.

Dingwell, D.B., Virgo, D., 1987. The effect of oxidation state on the viscosity of melts in the system Na_2O–FeO–Fe_2O_3–SiO_2. Geochim. Cosmochim. Acta 51, 195–205.

Giordano, D., Dingwell, D., 2003. Viscosity of hydrous Etna basalt: implications for Plinian-style basaltic eruptions. Bull. Volcanol. 65, 8–14.

Giordano, D., Nichols, A., Potuzak, M., Di Genova, D., Romano, C., Russell, J., 2015. Heat capacity of hydrous trachybasalt from Mt Etna: comparison with $CaAl_2Si_2O_8$ (An)–$CaMgSi_2O_6$ (Di) as basaltic proxy compositions. Contrib. Mineral. Petrol. 170, 1–23.

Giordano, D., Polacci, M., Longo, A., Papale, P., Dingwell, D., Boschi, E., Kasereka, M., 2007. Thermo-rheological magma control on the impact of highly fluid lava flows at Mt. Nyiragongo. Geophys. Res. Lett. 34. https://doi.org/10.1029/2006GL028459.

Giordano, D., Potuzak, M., Romano, C., Dingwell, D.B., Nowak, M., 2008a. Viscosity and glass transition temperature of hydrous melts in the system $CaAl_2Si_2O_8$–$CaMgSi_2O_6$. Chem. Geol. 256, 203–215.

Giordano, D., Russell, J.K., Dingwell, D.B., 2008b. Viscosity of magmatic liquids: a model. Earth Planet. Sci. Lett. 271, 123–134.

Gualda, G.A., Ghiorso, M.S., 2015. MELTS_Excel: a Microsoft Excel-based MELTS interface for research and teaching of magma properties and evolution. Geochem. Geophys. Geosyst. 16, 315–324.

Hamilton, D., Burnham, C.W., Osborn, E., 1964. The solubility of water and effects of oxygen fugacity and water content on crystallization in mafic magmas. J. Petrol. 5, 21–39.

Harris, A.J., Rowland, S., 2001. FLOWGO: a kinematic thermo-rheological model for lava flowing in a channel. Bull. Volcanol. 63, 20–44.

Harris, A., Rowland, S., 2009. Effusion-rate controls on lava flow length and the role of heat loss: a review. Studies in volcanology: the legacy of George Walker. In: Special Publications of IAVCEI, vol. 2, pp. 33–51.

Keszthelyi, L., Self, S., 1998. Some physical requirements for the emplacement of long basaltic lava flows. J. Geophys. Res., Solid Earth 103, 27447–27464.

Kolzenburg, S., Favalli, M., Fornaciai, A., Isola, I., Harris, A.J.L., Nannipieri, L., Giordano, D., 2016a. Rapid updating and improvement of airborne LIDAR DEMs through ground-based SfM 3-D modeling of volcanic features. IEEE Trans. Geosci. Remote Sens., 1–13. https://doi.org/10.1109/TGRS.2016.2587798.

Kolzenburg, S., Giordano, D., Cimarelli, C., Dingwell, D.B., 2016b. In situ thermal characterization of cooling/crystallizing lavas during rheology measurements and implications for lava flow emplacement. Geochim. Cosmochim. Acta.

Kolzenburg, S., Giordano, D., Thordarson, T., Höskuldsson, A., Dingwell, D.B., 2017. The rheological evolution of the 2014/2015 eruption at Holuhraun, central Iceland. Bull. Volcanol. 79, 45.

La Spina, G., Burton, M., Vitturi, M.D.M., 2015. Temperature evolution during magma ascent in basaltic effusive eruptions: a numerical application to Stromboli volcano. Earth Planet. Sci. Lett. 426, 89–100.

La Spina, G., Burton, M., Vitturi, M.D.M., Arzilli, F., 2016. Role of syn-eruptive plagioclase disequilibrium crystallization in basaltic magma ascent dynamics. Nat. Commun. 7, 13402.

Llewellin, E., Manga, M., 2005. Bubble suspension rheology and implications for conduit flow. J. Volcanol. Geotherm. Res. 143, 205–217.

Mader, H.M., Llewellin, E.W., Mueller, S.P., 2013. The rheology of two-phase magmas: a review and analysis. J. Volcanol. Geotherm. Res. 257, 135–158.

Markl, G., Marks, M.A., Frost, B.R., 2010. On the controls of oxygen fugacity in the generation and crystallization of peralkaline melts. J. Petrol. 51, 1831–1847.

Mollo, S., Giacomoni, P., Coltorti, M., Ferlito, C., Iezzi, G., Scarlato, P., 2015. Reconstruction of magmatic variables governing recent Etnean eruptions: constraints from mineral chemistry and P–T–fO_2–H_2O modeling. Lithos 212, 311–320.

Mysen, B.O., Virgo, D., Neumann, E.-R., Seifert, F.A., 1985. Redox equilibria and the structural states of ferric and ferrous iron in melts in the system CaO–MgO–Al_2O_3–SiO_2–FeO; relationships between redox equilibria, melt structure and liquidus phase equilibria. Am. Mineral. 70, 317–331.

Mysen, B.O., Virgo, D., Seifert, F.A., 1984. Redox equilibria of iron in alkaline earth silicate melts; relationships between melt structure, oxygen fugacity, temperature and properties of iron-bearing silicate liquids. Am. Mineral. 69, 834–847.

Nicolas, A., Ildefonse, B., 1996. Flow mechanism and viscosity in basaltic magma chambers. Geophys. Res. Lett. 23, 2013–2016.

Papale, P., 1999. Strain-induced magma fragmentation in explosive eruptions. Nature (London) 397, 425–428.

Pinkerton, H., Sparks, R.S.J., 1978. Field measurements of the rheology of lava. Nature 276, 383–385.

Poe, B.T., Romano, C., Di Genova, D., Behrens, H., Scarlato, P., 2012. Mixed electrical conduction in a hydrous pantellerite glass. Chem. Geol. 320, 140–146.

Robert, G., Russell, J.K., Giordano, D., Romano, C., 2008. High-temperature deformation of volcanic materials in the presence of water. Am. Mineral. 93, 74–80.

Russell, J., Giordano, D., Dingwell, D., 2003. High-temperature limits on viscosity of non-Arrhenian silicate melts. Am. Mineral. 88, 1390–1394.

Sato, H., 2005. Viscosity measurement of subliquidus magmas: 1707 basalt of Fuji volcano. J. Mineral. Petrol. Sci. 100, 133–142.

Sato, M., 1978. Oxygen fugacity of basaltic magmas and the role of gas-forming elements. Geophys. Res. Lett. 5, 447–449.

Schauroth, J., Wadsworth, F.B., Kennedy, B., von Aulock, F.W., Lavallée, Y., Damby, D.E., Vasseur, J., Scheu, B., Dingwell, D.B., 2016. Conduit margin heating and deformation during the AD 1886 basaltic Plinian eruption at Tarawera volcano, New Zealand. Bull. Volcanol. 78, 12.

Shaw, H., Wright, T., Peck, D., Okamura, R., 1968. The viscosity of basaltic magma; an analysis of field measurements in Makaopuhi lava lake, Hawaii. Am. J. Sci. 266, 225–264.

Sigurdsson, H., Houghton, B., McNutt, S., Rymer, H., Stix, J., 2015. The Encyclopedia of Volcanoes. Elsevier.

Spataro, W., Avolio, M.V., Lupiano, V., Trunfio, G.A., Rongo, R., D'Ambrosio, D., 2010. The latest release of the lava flows simulation model SCIARA: first application to Mt Etna (Italy) and solution of the anisotropic flow direction problem on an ideal surface. Proc. Comput. Sci. 1, 17–26.

Toplis, M., Carroll, M., 1995. An experimental study of the influence of oxygen fugacity on Fe–Ti oxide stability, phase relations, and mineral-melt equilibria in ferro-basaltic systems. J. Petrol. 36, 1137–1170.

Vetere, F., Rossi, S., Namur, O., Morgavi, D., Misiti, V., Mancinelli, P., Petrelli, M., Pauselli, C., Perugini, D., 2017. Experimental constraints on the rheology, eruption and emplacement dynamics of analog lavas comparable to Mercury's northern volcanic plains. J. Geophys. Res., Planets. https://doi.org/10.1002/2016JE005181.

Vona, A., Romano, C., 2013. The effects of undercooling and deformation-rates on the crystallization kinetics of Stromboli and Etna basalts. Contrib. Mineral. Petrol. 166, 491–509.

Vona, A., Romano, C., Dingwell, D.B., Giordano, D., 2011. The rheology of crystal-bearing basaltic magmas from Stromboli and Etna. Geochim. Cosmochim. Acta 75, 3214–3236.

Wilke, M., 2005. Fe in magma—an overview. Ann. Geophys. https://doi.org/10.4401/ag-3222.

Witter, J.B., Harris, A.J., 2007. Field measurements of heat loss from skylights and lava tube systems. J. Geophys. Res., Solid Earth (1978–2012) 112.